Building and Environment 223 (2022) 109493

Contents lists available at ScienceDirect

Building and Environment

journal homepage: www.elsevier.com/locate/buildenv

Removal of ultrafine particles in a full-scale two-stage electrostatic precipitator employing a carbon-brush ionizer for residential use

Sehyun Kim [a], Kiwoong Park [a], Changyoung Choi [b], Man Yeong Ha [a,**], Donggeun Lee [a,*]

[a] School of Mechanical Engineering, Pusan National University, 2 Busandaehak-ro, 63beon-gil, Geumjeong-gu, Busan, 46241, Republic of Korea
[b] Air Solution CAE Team, Air Solution R&D Lab., LG Electronics, 84 Wannam-ro, Seongsan-gu, Changwon-si, Gyeongsangnam-do, 51554, Republic of Korea

ARTICLE INFO

Keywords:
Two-stage electrostatic precipitator
Carbon-brush ionizer
Dielectric separator
Ultrafine particle removal
Simulation and experiment

ABSTRACT

Despite recent advances in the area of industrial electrostatic precipitators (ESPs), their residential use remains uncertain owing to the concern about ozone emissions when the removal efficiency of fine and ultrafine particles is increased. In this study, we propose a comprehensive numerical simulation of a full-scale two-stage ESP equipped with a carbon-brush ionizer that is capable of efficiently removing ultrafine particles with minimal ozone emissions. We calculated the spatial distributions of the electric potential and ionic charge density, the turbulent gas flow field coupled with ionic currents, and charge states and behavior of ultrafine particles in the entire region of the ESP. However, we did not investigate the ozone emission from the ionizer. In addition, we built an identical system to measure the profile of the local ionic current at the bottom of the discharging zone as well as the particle-collection efficiency. We clarified the effects of the orientation of the carbon brush tip and gas flow on the behavior of the ions and explored the behavior of charged particles in the collection unit with the insertion of a dielectric separator, thereby preventing air breakdown and increasing collection efficiency. All the simulation results were found to be consistent with experiments. We determined that a single carbon-brush electrode was sufficient to remove ultrafine particles at an efficiency of approximately 100% at 225 m^3/h.

1. Introduction

PM 2.5 has been recognized globally as a serious hazard to human health, both indoors and outdoors. Particle pollution can severely affect babies, children, and older adults. It is also challenging to control particulate contamination during the semiconductor manufacturing processes. In response to this, the Korean government has recently established what is termed the "Comprehensive Plan on Fine Dust Management" to reduce PM2.5 emissions by 35.8% from the 2014 level by 2022.

Many studies have sought to develop devices for fine particle removal. Among these, the high-efficiency particulate air (HEPA) filter is the most commonly used device in residential air purification systems. However, HEPA filters should be replaced periodically because the pressure drop across the filter media increases over time. In the semiconductor industry, wet scrubbers are used to remove contaminants from waste gases [1]. Wet scrubbers are generally efficient for soluble corrosive gases removal; however, they have limited use in PM 2.5 dust removal. They also require large installation space [2,3]. Electrostatic precipitator (ESP) invented by Smith and Cottrell [4] in 1989 can run with high particle-collection efficiency, low air resistance, and low maintenance cost compared with aforementioned methods.

ESP phenomena can be understood by analyzing three physical dynamics during the typical operating conditions of these devices. These include turbulent gas flow, ionic currents generated by electrostatic fields, and the charging and motion of the particles [5]. In particular, an additional body force generated by the electric potential and ionic charge density activates the secondary electro-hydrodynamic (EHD) flow of the gas [6]. In addition, the charge density can affect the distribution of the electrical potential owing to the space-charge effect. These mutual interactions between the three different phases make the ESP phenomenon a complex multiphysics problem. Starting with the pioneering work of McDonald et al. to develop a mathematical model [7], many researchers have investigated multi-physical phenomena associated with ESPs through experimental studies and numerical simulations. Some of these studies are discussed below.

Nikas et al. [8] numerically investigated the electrostatic field, gas flow, and particle motion characteristics of a wire-plate single-stage ESP where the charging and collection of particles occur simultaneously.

* Corresponding author.
** Corresponding author.
E-mail addresses: myha@pusan.ac.kr (M.Y. Ha), donglee@pusan.ac.kr (D. Lee).

https://doi.org/10.1016/j.buildenv.2022.109493
Received 9 April 2022; Received in revised form 28 July 2022; Accepted 10 August 2022
Available online 17 August 2022

Nomenclature

Symbols

C_c	Cunningham slip correction factor
D_{ion}	Diffusivity of ions (m^2/s)
d_p	Particle diameter (m)
e	Elemental charge of electron (1.6×10^{-19} C)
E	Electric field strength (V/m)
E_{dis}	Critical field strength for corona onset (V/m)
E_i	Component of electric field strength (V/m)
F_{coul}	Coulomb force on particles per unit mass of particles (m/s^2)
F_D	Slip-corrected friction factor per unit mass of particles (1/s)
g	Gravity acceleration (m/s^2)
k_b	Boltzmann constant (1.38×10^{-23} J/K)
k_{iom}	Electrical mobility of ions (m^2/V s)
L_{pl}	Length of dust-collecting plate (m)
m_p	Mass of particles (kg)
n	Spread parameter
P	Pressure (Pa)
p_{pl}	Pitch of dust-collecting plate (m)
q_p	Charge of particles (C)
r	Radius of the discharge electrode (m)
T	Temperature (K)
t	Time (s)
t_q	Dimensionless charging time
u	Velocity of air (m/s)
u_i, u_j	Velocity component of air (m/s)
u_p	Velocity of particles (m/s)
V_{in}	Velocity of gas at the inlet of discharging zone (m/s)
v	Dimensionless particle charge
w	Dimensionless electric field strength
x_i, x_j	Coordinate (m)
Y_d	Mass fraction with diameter greater than d_p

Greek letters

δ	Relative density of gas
ϵ_0	Air permittivity (8.85×10^{-12} F/m)
ϵ_r	Dielectric constant of particles
φ	Local electric potential (V)
φ_{pl}	Electrical potential on dust-collecting plate (V)
λ	Mean free path of air (m)
μ	Dynamic viscosity of air (kg/m s)
ν	Dimensionless particle charge
ρ_f	Density of air (kg/m^3)
ρ_p	Density of particles (kg/m^3)
ρ_{ion}	Charge density of ions (C/m^3)
N_{ion}	Number density of ions (C/m^3)

These processes were calculated by time integration of the motion and charging rate equations of particles of a certain size. Taking a Lagrangian approach by monitoring a large numbers of particle trajectories is clearly an accurate way to predict particle-collection efficiency. However, their numerical simulations were validated only for coarse particles with a diameter of 4–9 μm that are subject to field charging, indicating the need to incorporate diffusion charging for ultrafine particles, such as in the particle-charging model proposed by Lawless [9]. Recently, a simulation model was implemented in the commercial CFD software FLUENT using user-defined functions (UDFs) for ease of use in more advanced designs of wire-plate single-stage ESPs, such as an inline vs staggered arrangement of ionizing wires [10] and a flat vs wavy configuration of particle-collecting plates [11].

A single-stage ESP can typically process massive flows of dusty air with a simple structure, which accounts for its popularity in industrial applications dealing with coarse particles. However, it is not suitable for residential applications because of its high ozone emissions and poor performance in removing fine and ultrafine particles. In contrast, a two-stage ESP is better at the optimal charging of fine particles with lower charging voltages given separate discharging and collection units [12]. This has led to a series of experimental and numerical simulation studies, starting with wire-plate two-stage ESPs to design changes in the gas ionizer or collecting plates, as described below.

Gao et al. [12] conducted experimental and numerical simulation studies of the collection efficiency of fine particles (0.4–2 μm) in a wire-plate two-stage ESP operating under different gas flow velocities (0.5–2 m/s). It was found that the collection efficiency was only 28% for 0.4 μm particles, both in a simulation and in an experiment, whereas the gas flow field was barely influenced by the EHD flow except near the wire electrode. Zhu et al. [13] in the same group reported a new design of W-shaped collection plates that could increase the collection efficiency to approximately 100% for fine particles (0.3–1 μm) with a charging voltage of 8 kV. However, the gas flow rate was as low as 0.17 cubic meters per hour (CMH), implying that a large number of wire electrodes would be required for full-scale residential applications, with CMH rates typically approaching at least several hundred. Apart from these trials, another experimental approach in Korea was to insert dielectric separators into the collection plates with the aim of increasing both the air breakdown voltage and dust removal efficiency. Kim et al. [14,15] demonstrated that the existence of a dielectric layer between successive collection plates was clearly beneficial for increasing the collection efficiency of 300 nm particles, but did not explain the reason.

Another line of research on two-stage ESPs relates to the ozone issue involving a change of the electrode material from metal to carbon. Carbon fibers 2–5 μm in diameter are often available in the form of a fiber bundle (also called a "carbon brush") in the market. Carbon brushes provide similar collection efficiencies with a lower charging voltages as compared to those with the wire-plate type [16]. For instance, Kim et al. [17] developed a two-stage ESP with a carbon-brush ionizer to investigate diffusion charging and collection efficiency of ultrafine particles (0.02–0.4 μm). The collection (or charging) efficiency was affected when an additional voltage was applied to the duct wall surface to which the carbon brush was connected. This shows the significance of the behavior of ions in the charging stage. Up to 90% average collection efficiency was achieved with two successive carbon-brush ionizers at a flow rate of 6.6 CMH, corresponding to an average air flow 0.19–0.23 m/s (only a quarter of typical speeds). They upgraded the two-stage ESP unit by adding up to 18 carbon-brush ionizers in the charging stage, demonstrating collection efficiency rates that remained above 90% at gas flow rates in the range of 36–90 CMH [18]. In their next experimental study [19], a new pilot-scale ESP with multiple carbon-brush ionizers was installed in a test chamber 30 m^3 in size to spray gaseous ions into the chamber. The resulting clean air delivery rate (CADR) was 7.32 m^3/min, indicating that 90% of the *charged* submicron particles were collected in the ESP within 16 min with negligible ozone emission (1.3 ppb for 12 h). However, prior to switching on the ESP, the chamber was initially filled with both particles and ions. This allowed the particles to have an unrealistically long time for diffusion charging, compared to the short residence time of ions (~1 s) flowing through typical ESPs. Thus, the result might be considered, as the upper limit achieved by ESP. To the best of our knowledge, a direct numerical simulation of a two-stage ESP equipped with carbon-brush ionizers has not been conducted thus far. In fact, there are only a few simulation studies of needle-plate or -ring ionizers, which are similar in shape to

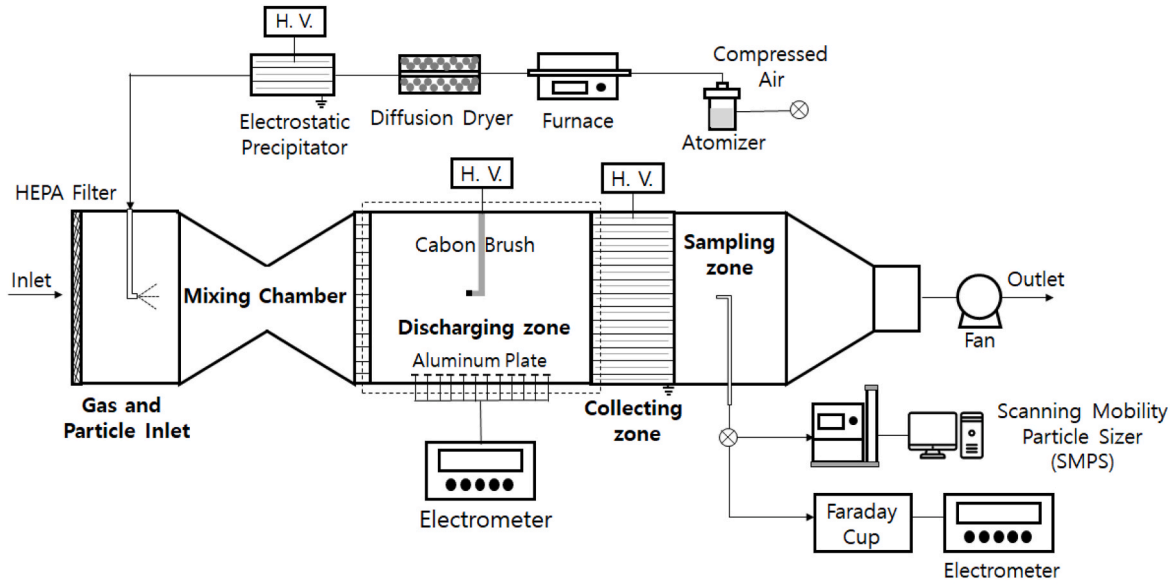

(a)

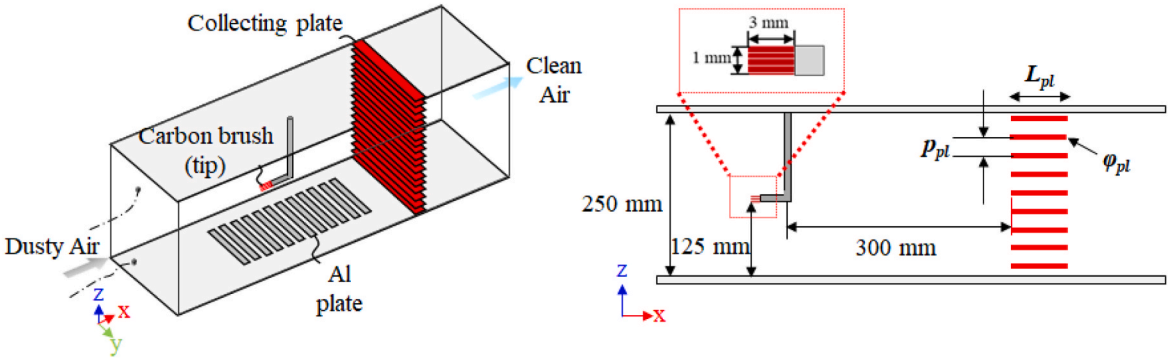

(b)

Fig. 1. Experimental apparatus: (a) Schematic of the entire experimental system including the present two-stage electrostatic precipitator, (b) Isometric and side views of the internal structure of the discharging zone and the collecting zone.

carbon-brush ionizers. Sattari et al. [20] simulated the electric field and charge density distribution from a sharp needle-plate ionizer, with stationary air by solving the Poisson equation with a custom-made code. Guan et al. [21] performed numerical simulations based on FLUENT to obtain the distributions of the electric field, gas flow field, and ionic charge density, but only inside a tungsten needle-ring ionizer focusing on ionic transport and the resulting EHD flow. Zheng et al. [22] calculated the temporal number variations of electrons and positive and negative ions inside a needle-plate discharger and showed that a sharper needle with a smaller tip radius is more advantageous for increasing the ionic current under a constant charging voltage. Park et al. [23] performed a comprehensive numerical simulation based on FLUENT to calculate the electric field, gas flow field, charging and trajectory characteristics of ultrafine particles in a micro-machined metallic spike-plate ionizer. Technically, their numerical simulations are comparable to those in a wire-plate single-stage ESP [10,11]; however, their findings are limited to unipolar charging phenomena in a microchannel flow, which are primarily laminar.

One may conclude that there is an urgent need for a highly advanced two-stage ESP with carbon-brush ionizers that is appropriate for residential use; however, none of the existing studies involving numerical simulations are applicable because of discrepancies in gas flow rates, the design of the discharging electrodes, and the sizes of the target particles. Even in experimental studies, questions remain about the discharge characteristics and applicability of carbon-brush electrodes under the typical operating conditions of two-stage residential ESPs.

Thus, the objective of this study was to implement a comprehensive numerical simulation to calculate the spatial distributions of the electric potential and ionic charge density, turbulent gas flow field coupled with the ionic current, and charge states and behavior of ultrafine particles in an entire full-scale two-stage ESP by expanding our previous simulations of single-stage ESPs [10,11]. To validate the simulations, we devised a full-scale air duct system in which a single carbon-brush discharger and particle-collecting plates were installed in series. It was ensured that the exact boundary conditions in the experiment were in accordance with the simulations. Specifically, the profile of the ionic current density measured at the wall of the duct was compared with the simulated profile in both the absence and presence of a gas flow at 225 CMH. The role of the orientation of the carbon-brush tip in the ionic currents was examined. In addition, we investigated the charged particle behavior

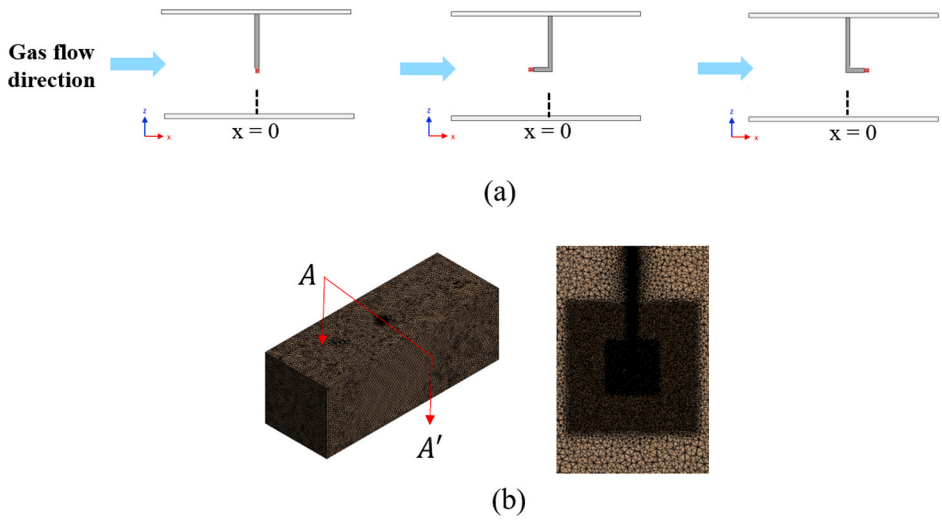

Fig. 2. (a) Three different orientations of the carbon brush tip and (b) A typical computational grid system generated for the discharging zone.

and collection efficiency based on various design parameters.

2. Numerical simulation method and experimental verification

2.1. Experimental set up for validation

Fig. 1(a) shows a schematic of the experimental system. This includes the test section of the present two-stage ESP, an ultrafine-particle generation unit, a group of measurement devices for size distributions and charge states of ultrafine particles, and electrical currents of ions. The test section consisted of a gas/particle inlet, mixing chamber, discharging zone, collecting zone, sampling zone, and induction fan (see Fig. S1(a) in the Supplementary Data). A flow straightener was installed upstream of the HEPA filter in the gas/particle inlet, whereas a fine mesh was installed just ahead of the fan to ensure a spatially uniform air flow over each cross-section. A collision-type home-made atomizer and a silica-gel diffusion dryer were used to generate ultrafine KCl particles using a spray-drying method at 0.3 CMH. To avoid any unexpected effects of the initial charge of the as-produced particles, an extra ESP working at 5.2 kV was connected to the dryer exit to permit only uncharged particles to pass. Then, the aerosol particles were introduced into the (left-most) gas/particle inlet of the system, in which filtered air flowed at 225 CMH. The particles were then spatially homogenized while passing through the mixing chamber prior to entering the discharging zone.

Fig. 1(b) shows the internal structure of the discharging and collecting zones. In the discharging zone, a circular carbon-brush electrode (3 mm long and 1 mm thick) was connected to a plastic coated electrical wire. To ensure that the surface electric potential remained at zero, the plastic coating on the surface of the wire electrically grounded after being covered with a thin layer of aluminum foil. The external surface of the discharging zone was treated similarly to ensure that it remained grounded. The intent was to induce a corona discharge between the tip of the carbon brush and the external surface. As such, on applying a negative high voltage (−7.7 kV) to the carbon brush, negative ions are generated from the tip; these ions move toward the surrounding walls of the zone (duct) owing to the electric field. Each wall was made of an acrylic plate that served as an electrical insulator. 15 aluminum plates, each is 10 cm long and 1 cm wide, were attached at intervals of 1 cm on the bottom (inner) surface of this zone (see the picture of the aluminum plates in Fig. S1(b)). Thus, the ions collected on each plate could be measured as an electrical current using a sensitive electrometer (Keithley 6430). The current value was divided by the area of the plate to obtain the ionic current density at each local position at the bottom. This measurement was repeated three times for each condition to ensure experimental repeatability. In addition, an experiment on the ionic current density distribution was performed twice with and without the air flow to clarify the effect of airflow on the behavior of ions in the discharging zone. Before this experiment all aluminum plates and inner duct surface were cleaned with ethanol to prevent unexpected contamination and remove any residual ions.

Particles flowing through the discharging zone can be field charged and/or diffusion charged by the corona discharge. Unlike ions, heavier charged particles are not affected by the electric field in the discharging zone, implying that they enter the collection zone without affecting it. A set of multiple collection plates were installed to fit the entire cross-section (25 cm × 25 cm) of the duct; each plate was 3.6 cm × 25 cm and was horizontally positioned with a spacing of 2 or 3 mm (see Fig. 1 (b)). If −5.2 kV is applied to every second plate while the other plates are grounded, charged particles are forced to attach to the grounded plates. At the exit of the collection zone (see the sampling zone in Fig. 1(a)), the dusty air flow was sampled to measure the total number concentrations and size distributions of the particles in the range of 0.015–0.65 μm with a scanning mobility particle sizer (SMPS; Model 3936, TSI Corp). We also measured the electrical current of the charged particles using a Faraday cup and a sensitive electrometer (Keithley 6430). The number concentration was monitored by switching the collection voltage on and off, yielding the collection efficiency of the ESP. Simultaneously, the measured electrical current of charged particles was compared with the flow rates of the particles in units of #/s, allowing us to determine the average charge of the particles. Further details about the instrumentation used for the particle generation and measurement processes are available in our previous publications [24,25].

2.2. Numerical simulation

The calculation domain of the numerical simulation was set to be identical to that of the two-stage ESP illustrated in Fig. 1(b). In the present simulations and experiments, we considered three different orientations of the carbon-brush tip as shown in Fig. 2(a). As shown in Fig. 1(b), a left-facing bent carbon brush was installed 12.5 cm away from the bottom of the duct while the dusty air was set to flow from left to right. For the right-facing or downward-facing carbon brush, the tip was consistently positioned at the same height from the bottom, but at the different x locations with respect to the extension wire of the carbon brush (see Fig. 2(a)). Fig. 2(b) shows an example of a typical grid system for the discharging zone. The dust-collecting plate was installed 300 mm from the extension wire of the carbon brush and had three design

Table 1
Summary of boundary conditions used in the present study.

Boundary	Gas flow [m/s]	Electric potential [kV]	Current density [A/m^2]
Inlet	u	0	$\frac{\partial \rho}{\partial n}$
Outlet	Pressure outlet	0	$\frac{\partial \rho}{\partial n}$
Wall duct	No slip	0	$\frac{\partial \rho}{\partial n}$
Carbon brush tip	No slip	7.7	4×10^{-5}
Carbon brush side	No slip	7.7	0

Table 2
Summary of physical properties of used in the present study.

ρ_f [kg/m^3]	μ [kg/ms]	T [K]	ϵ_0 [C^2/Nm]	k_{ion} [m^2/Vs]	D_e [m^2/s]	ϵ_r
1.24	1.79×10^{-5}	288.2	8.85×10^{-12}	1.4×10^{-4}	3.98×10^{-6}	2.93

parameters: plate spacing (p_{pl}), plate length (L_{pl}), and applied voltage (φ_{pl}). The dimensions of the design parameters shown in Fig. 1(b) for the simulations were identical to those for the experiments. All variables and constants in the following equations comply with the International System of Units unless otherwise noted (refer to Nomenclature).

Because most two-stage ESP systems do not generate any discernible pressure loss or temperature gradient, the gas flow was considered an incompressible turbulent flow, as described by the following mass and momentum conservation equations.

Equation of continuity:

$$\frac{\partial}{\partial x_i}\left(\rho_f u_i\right) = 0 \tag{1}$$

Equation of momentum:

$$\frac{\partial}{\partial x_j}\left(\rho_f u_i u_j\right) = -\frac{\partial P}{\partial x_i} + \frac{\partial}{\partial x_j}\left[\mu\left(\frac{\partial u_i}{\partial x_j} + \frac{\partial u_j}{\partial x_i}\right) - \rho_f \overline{u_i' u_j'}\right] + E_i \rho_{ion} \tag{2}$$

In these equations, $E_i\rho_{ion}$ represents the body force, which creates the effect of ionic wind on the gas flow. A standard $k-\varepsilon$ turbulence model and a standard wall function model were used to calculate the Reynolds stress, $-\rho_f \overline{u_i' u_j'}$. The lack of particle-induced drag force in Eq. (2) proves that most indoor aerosol particles are indeed submicron particles under

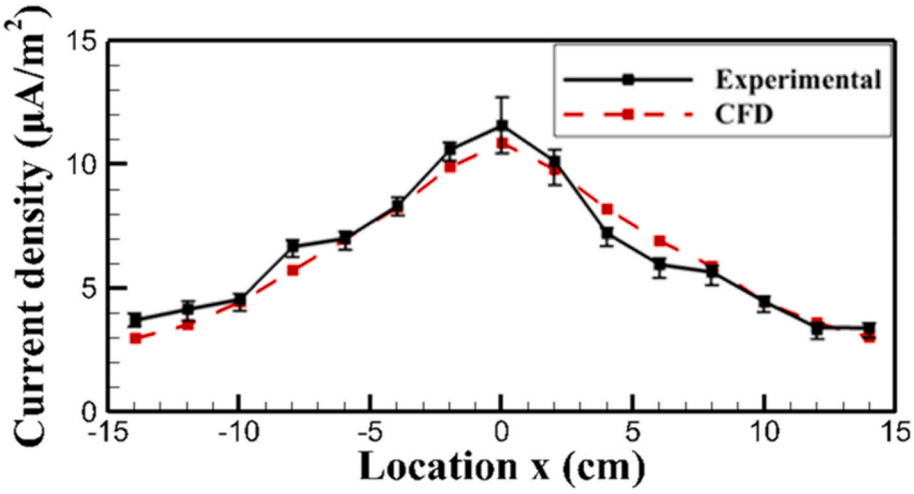

(a)

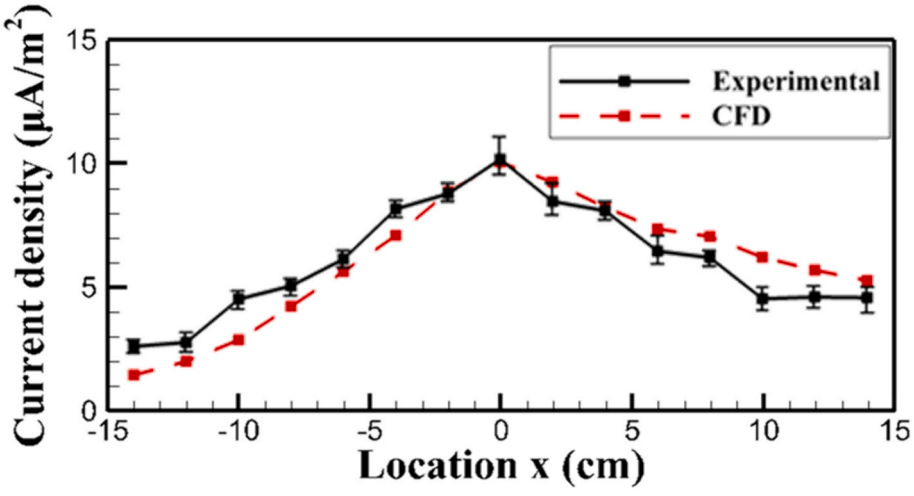

(b)

Fig. 3. Comparison of ionic current density profiles measured at the bottom plate between the numerical simulation and the experiment when the brush tip faces downward: (a) $V_{in} = 0$ m/s and (b) $V_{in} = 1$ m/s.

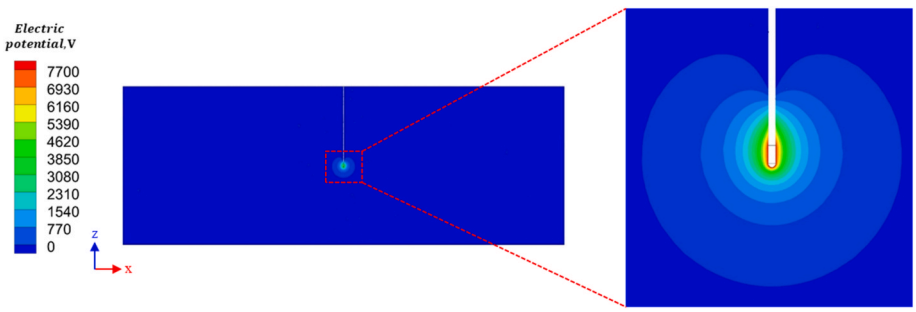

Fig. 4. Contour plot of electric potential in the discharging zone; the inset highlights near-spherical iso-potential lines in the vicinity of the carbon brush tip.

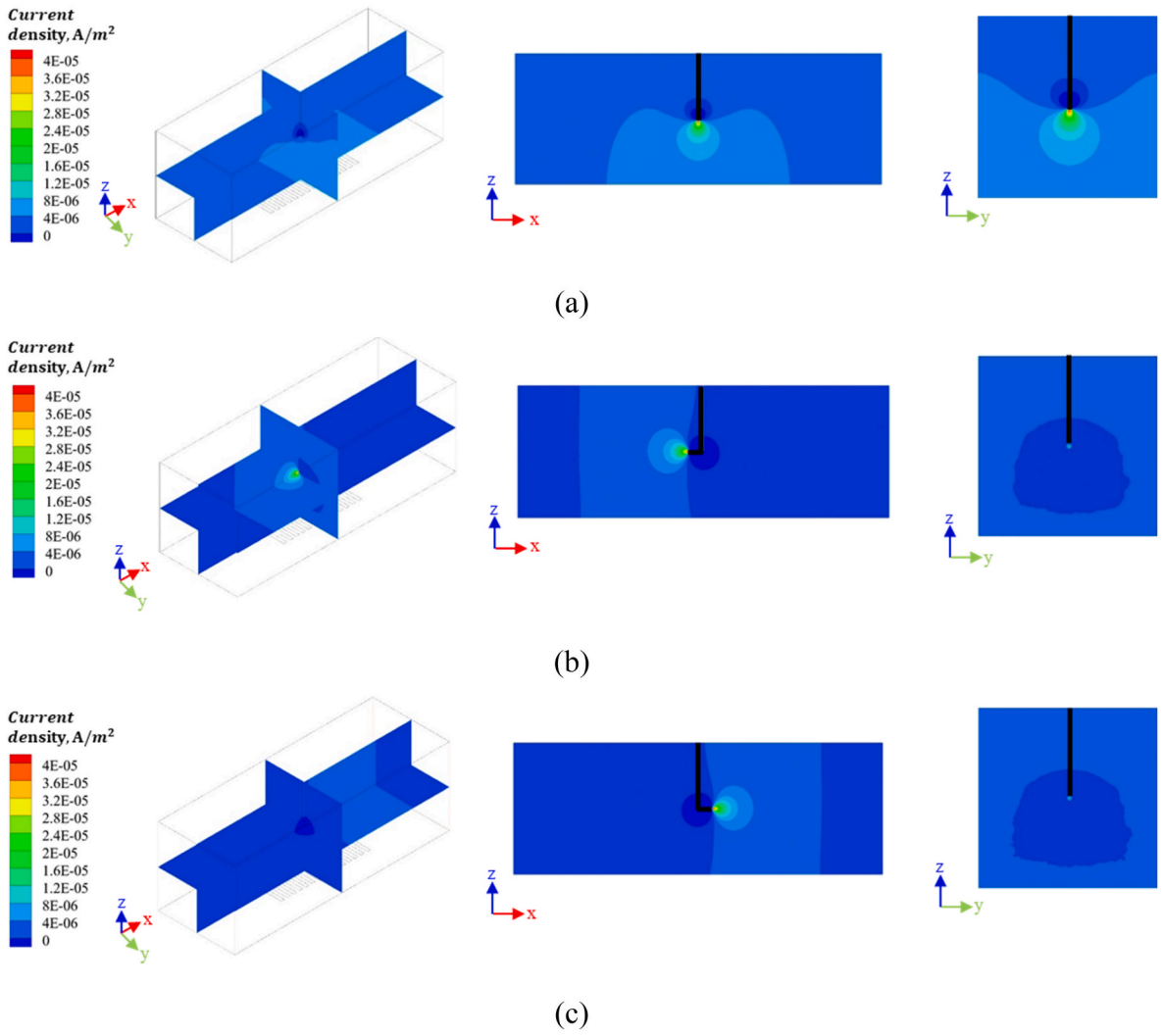

Fig. 5. Contour plot of local ionic current density at $V_{in} = 0$ m/s for three different orientations of the carbon brush tip: (a) Downward-facing, (b) Left-facing, and (c) Right-facing.

dilute conditions such that the turbulent gas flow was only one-way coupled with the behaviors of particles [26].

The electric field and ionic current inside the current ESP are determined by solving the Poisson equation and charge transport equation, as follows:

Poisson equation:

$$\frac{\partial^2 \varphi}{\partial x_i^2} = -\frac{\rho_{ion}}{\varepsilon_0} \tag{3}$$

Charge transport equation:

$$\frac{\partial}{\partial x_i}\left[\rho_{ion}(k_{ion}E_i + u_i) - D_{ion}\frac{\partial \rho_{ion}}{\partial x_i}\right] = 0 \tag{4}$$

where φ and E_i are the local electric potential and electric field strength in space, respectively; ρ_{ion}, k_{ion}, and D_{ion} are the charge density, electrical mobility, and diffusivity of ions; and ε_0 is the permittivity of air. The electric field strength distributions can be calculated from the potential gradient using the following equation:

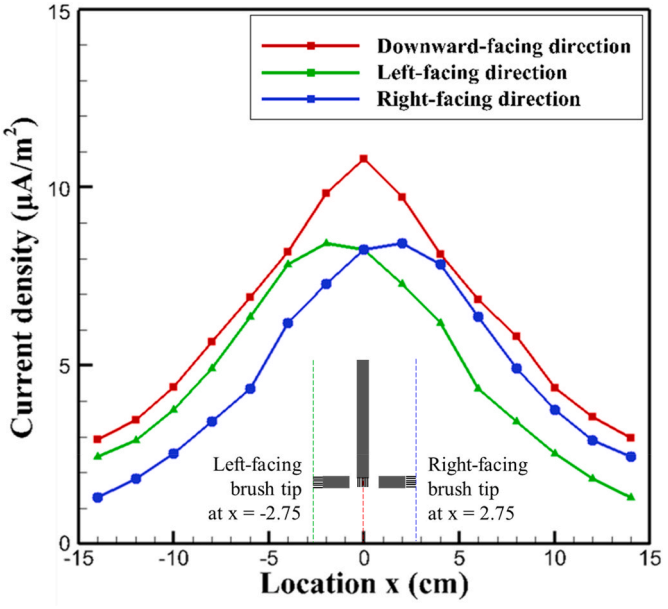

Fig. 6. Distribution of the current density measured on the bottom floor of the discharging zone for the different orientations of the carbon brush tip when V_{in} = 0 m/s.

$$E_i = -\frac{\partial \varphi}{\partial x_i} \tag{5}$$

Because of the nature of the Poisson equation, the isopotential curves were concentrated on the sharp edge of a discharging electrode akin to a carbon brush tip, resulting in a sharp increase in the local field strength. Air begins to break down to release gaseous ions when the field strength increases beyond a critical value. We used Peek's semi-empirical correlation [27] to determine the critical electric field strength for corona onset using:

$$E_{dis} = 3.1 \times 10^6 \delta \left(1 + \frac{0.03}{\sqrt{\delta r}}\right), \tag{6}$$

where δ is the relative density of gas with reference to the value under the standard condition; it can be approximated to unity under the typical operating conditions of the ESPs. Initially, r was originally set as the radius of the wire electrodes but was later replaced with the overall radius (0.5 mm) of the carbon brush used.

The unipolar charging of particles is usually described as a collision with the surrounding ions. Therefore, the charging rate of the particles is dependent on the relative population of ions per single particle, which explains why the electric field determining the local charge density of ions is interconnected with the particle sizes and the specific trajectories in the discharging zone. It is acknowledged that diffusion charging is adequate for small particles or a low electric field, whereas field charging is considered adequate for larger particles or a high electric field. However, our submicron particles pass through high and low electric fields depending on the distance from the carbon brush. Thus, the combined charging model proposed by Lawless [9] was used to encompass both charging regimes, as expressed in the non-dimensional form below:

Particle charging model:

$$\frac{dv}{dt_q} = \begin{cases} f(w)\dfrac{v - 3w}{\exp(v - 3w) - 1} & , v > 3w \\ \dfrac{3w}{4}\left(1 - \dfrac{v}{3w}\right)^2 + f(w) & , -3w \le v \le 3w \\ -v + f(w)\dfrac{-v - 3w}{\exp(v - 3w) - 1} & , v < -3w \end{cases} \tag{7}$$

$$f(w) = \begin{cases} \dfrac{1}{(w + 0.475)^{0.575}} & , w \ge 0.525 \\ 1 & , w < 0.525 \end{cases} \tag{8}$$

where $v(= q_p e/2\pi\varepsilon_0 d_p k_b T)$ is the dimensionless particle charge, $w(= (\varepsilon_r/\varepsilon_r + 2)(E d_p e/2k_b T))$ is the dimensionless electric field strength, $t_q(= \rho_{ion} k_{ion} t/\varepsilon_0)$ is the dimensionless charging time, and $f(w)$ represents the area fraction of the particle surface that receives the diffusion current of the ions. Table 1 lists the boundary conditions used for our numerical simulation, and Table 2 lists the physical properties of the gas and ions used in this study referring to the literature [9,28].

Once the particles are charged in the discharging zone, their subsequent motion is subject to drag force by the turbulent gas flow and electric force by the field particularly near the collection plates. In accordance with the methods devised by Nikas et al. [8], a Lagrangian approach was employed to simulate the trajectories of charged particles based on a discrete phase model (DPM) in FLUENT [10,11], defined as shown below.

Particle motion equation:

$$\frac{d\vec{u}_p}{dt} = F_D\left(\vec{u} - \vec{u}_p\right) + \vec{F}_{coul} \tag{9}$$

Coulomb's force equation:

$$\vec{F}_{coul} = \frac{q_p \vec{E}}{m_p} = \frac{6 q_p \vec{E}}{\pi \rho_p d_p^3} \tag{10}$$

In Eqs. (9) and (10), $F_D(\vec{u} - \vec{u}_p)$ and $\vec{F}_{coul}$ represent the drag force and Coulomb force acting on per unit mass of the particle, respectively; q_p, ρ_p, and d_p are the charge, density, and diameter of the particle, respectively; and F_D in Eq. (9) represents the slip-corrected friction factor for the Stokes drag [29] per unit mass of the particle, as expressed by

$$F_D = \frac{18\mu}{d_p^2 \rho_p C_c}, \tag{11}$$

where μ is the dynamic viscosity of the gas and C_c is the Cunningham slip correction factor for a gas with the mean free path (λ), as expressed by $C_c = 1 + (1.257 + 0.4e^{-(1.1 d_p/2\lambda)})(2\lambda/d_p)$ [30]. It is noted that no diffusive term is included in Eq. (9). According to Lindquist et al. [31], behaviors of ultrafine particles are determined by the two dimensionless parameters: the particle Knudsen number ($Kn_D = \sqrt{m_p k_B T}/f r_p$) and the advective motion factor defined by $\chi_F = m_p v_{ad}^2/k_B T$. For 0.05-μm particles (practically smallest in size), we calculated the two parameters as $Kn_D = 1.21 \times 10^{-2}$ and $\chi_F = 9.82 \times 10^{-3}$, corresponding to $\log(Kn_D) = -1.9$ & $\log(\chi_F) = -2.0$. Under this condition, one may notice that diffusive motion of the particles was found to be negligible (referring to Fig. 1 in Ref. [31]), which justifies the neglect of particle diffusion.

All the equations for charging and motion of the particles contain the term of the particle diameter d_p (see Eqs. (7)–(11)), which suggests that the size distribution of the particles is a key factor affecting collection efficiency. Therefore, we measured the size distribution of the pristine particles using SMPS at the sampling zone after grounding both the carbon brush and collection plates. The particle size ranged mostly from 0.05 μm to 0.5 μm with a mode diameter of ~0.1 μm, indicating that the size distribution is approximately lognormal (see Fig. S2 in the Supplementary Data). The size distribution, because it is based on numbers, was converted to the mass size distribution with the assumption of spherical KCl particles and then fitted to the Rosin–Rammler equation [32], defined as $\ln Y_d = -(d_p/\overline{d_p})^n$ for tracking the particles in FLUENT, where Y_d is the cumulative oversize mass fraction of particles greater than d_p, $\overline{d_p}$ is the mean diameter, and n is the spread parameter.

The collection efficiency was calculated in two different ways. First, thousands of particles (2022 in total) were randomly created in space

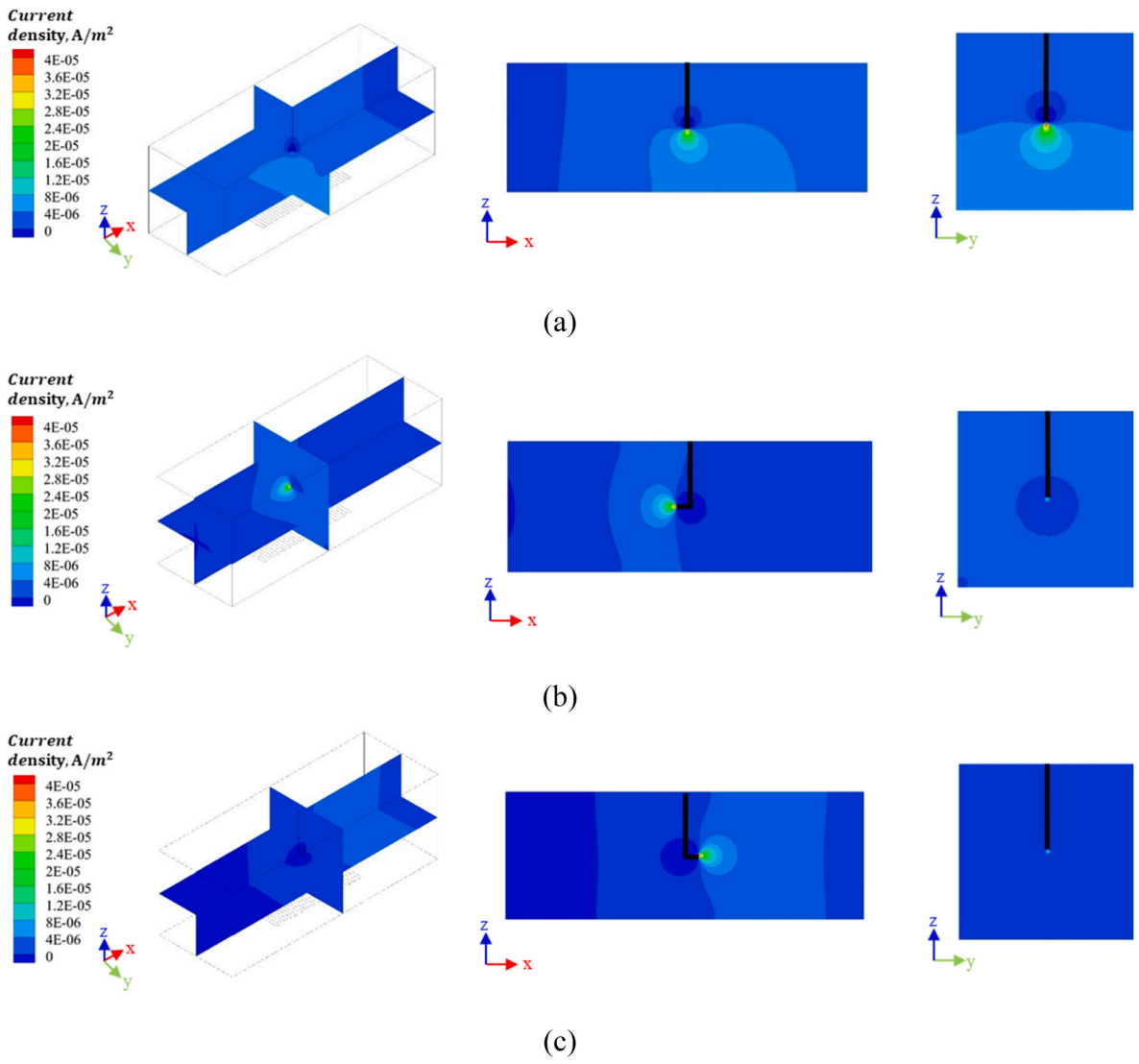

Fig. 7. Contour plot of local ionic current density at $V_{in} = 1$ m/s for three different orientations of the carbon brush tip: (a) Downward-facing, (b) Left-facing, and (c) Right-facing.

and in diameter on an artificial cross-section at the inlet of discharging zone, so as to ensure that those particles are unfirmly distributed on the cross-section and follow the size distribution. Each of the particles was then being traced up until they pass through or are captured in the collection plate. Then, the overall collection efficiency was simply calculated from the number fraction of captured particles with respect to the initial (total) number of particles launched to the space. Second, similarly thousands of particles of *a certain size* were created to launch at the same locations on the inlet cross-section and traced to calculate the collection efficiency for the size of the particles. This simulation was continued by altering the size of particles from 0.03 μm to 0.42 μm, which yield the size-resolved collection efficiency.

2.3. Validation of the present numerical simulations

A grid-dependency test was conducted to determine the appropriate number of grids for the numerical simulation. Fig. S3 in the Supplementary Data compares the ionic current densities measured at the bottom of the discharging zone for different total numbers of grids. When $V_{in} = 1$ m/s, doubling the total number of grids from 4.5 million to 8.5 million did not affect local current density. This allowed us to choose the middle number, i.e., 6.5 million for the remaining numerical simulations.

To validate our numerical simulation methodology, we measured the ionic current densities at 15 different locations at the bottom of the discharging zone, in accordance with the experimental procedure described in Section 2.1. As a preliminary experiment, we monitored the transient response of the ionic current density from a central aluminum plate located at the same horizontal position as the carbon brush tip ($x = 0$). A common trend observed in the experiments was that the current density increased sharply when the discharger is switched on and levelled out within 150–200 s to remain almost constant. This stabilized value was compared with that obtained from the numerical simulations.

Fig. 3 compares the current density distribution simulated at the bottom of the discharging zone with that obtained from the present experiment when the brush tip faces downward. The simulated results are consistent with the experimental data in both cases, that is, with and without gas flow. With stationary air ($V_{in} = 0$ m/s), Fig. 3(a) shows that the current density distribution was symmetric with respect to the vertical axis ($x = 0$) passing through the carbon brush tip. The ions emitted from the brush tip drift radially owing to the electric field, which is axisymmetric because of the configuration of the carbon brush. This may explain the volcano-shaped symmetric profile of the current density. In contrast, when the gas flows toward the right, the downward radiation

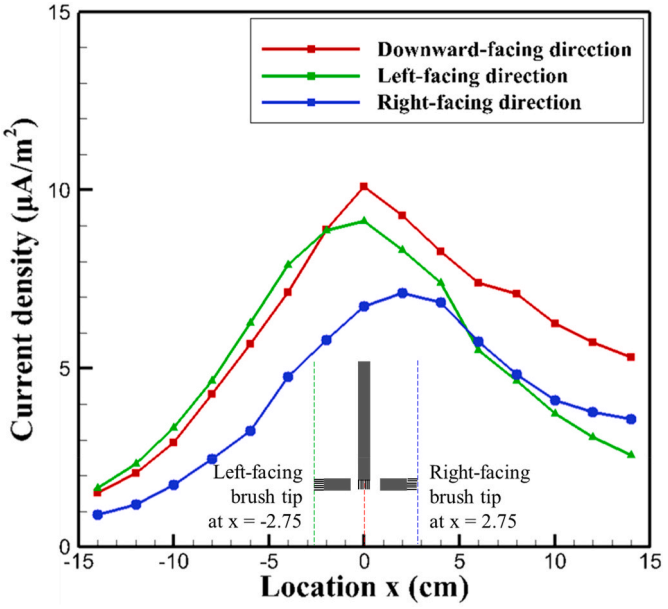

Fig. 8. Distribution of the current density measured on the bottom floor of the discharging zone for the different orientations of the carbon brush tip when V_{in} = 1 m/s.

Table 3
Design parameters of the particle collecting plates.

Design parameters					
Plate pitch (p_{pl})	–	$p_{pl,1}$	Baseline	$p_{pl,2}$	$p_{pl,3}$
	–	2 mm	**4 mm**	6 mm	8 mm
Plate length (L_{pl})	$L_{pl,1}$	$L_{pl,2}$	**Baseline**	$L_{pl,3}$	–
	10 mm	20 mm	**36 mm**	50 mm	–
Applied voltage (φ_{pl})	–	$\varphi_{pl,1}$	**Baseline**	$\varphi_{pl,2}$	$\varphi_{pl,3}$
	–	4.5 kV	**5.2 kV**	5.9 kV	6.6 kV

of ions to the bottom is expected to be biased toward the flow direction (refer to Eq. (4) where the charge density of the ions can be affected not only by the E-field drift velocity but also by the gas velocity). Fig. 3(b) indicates that a gas flow of 1-m/s was not as dominant as the ionic behavior inside the discharging zone because the symmetric profile was slightly skewed to the right, although the profile still peaked at the same position ($x = 0$).

3. Results and discussion

3.1. Effect of the orientation of the carbon brush tip on the ionic current in the discharging zone

The effect of brush tip orientation on the electrostatic field distribution was investigated by considering three different tip orientations: downward-facing, left-facing, and right-facing, as shown in Fig. 2(b).

Fig. 4 shows a contour plot of the electrical potential in the x-z section when the brush tip faces downward. When a high voltage is applied to the brush, the equipotential lines become highly concentrated at the carbon brush tip and become sparse away from the tip. Because the equipotential lines resemble concentric spheres 1 cm or farther away from the tip, any ions that reach this region are likely to move in the radial direction to cover the entire y-z cross-section. However, the inset of the figure indicates that the equipotential lines are attached more tightly to the brush tip than to its side, suggesting that the ions are more likely to form and are emitted from the tip downward, as if the carbon brush is directionally emitting ions.

Fig. 5 shows contour plots of the local ionic flux in units of A/cm^2, that is, the current density according to the three different orientations of the brush tip when $V_{in} = 0$ m/s. When the brush tip faces downward, as shown in Fig. 5(a), the current density shows left and right symmetry on both the x-z plane (front view) and the y-z cross-section (side view), which is consistent with the display in Fig. 3(a). We confirmed that the ionic currents are directed preferentially toward the bottom. Such directional emissions of ions from the carbon brush tip are observed in Fig. 5(b) and (c) for the left-facing and right-facing cases, respectively. For a quantitative comparison, we compared the local current density profile monitored at 15 different locations at the bottom of the three cases. Fig. 6 shows that the left-facing carbon brush tip skewed the symmetric profile to the right together with a 2-cm left shift of the peak, whereas the right-facing case showed the opposite trend, mirroring the profile with respect to the central axis ($x = 0$). In addition, Fig. 6 indicates that the current density profile for the left- or right-facing tip was shifted down relative to the profile for the downward-facing tip, indicating that the total ionic current to the bottom was the largest in the downward-facing case. However, the left- or right-facing tip provides a spatially-uniform ionic current over the cross-section of the duct, as evident from the up and down symmetry, as shown in Fig. 5(b) and (c). Therefore, a left- or right-facing carbon brush is recommended for efficient charging of ultrafine particles.

Compared with Figs. 5 and 7 highlights distinct differences in the current density distribution when the gas flows at $V_{in} = 1$ m/s. In Fig. 7 (a), the carbon brush tip faces downward, and ions that were originally drifting downward appear pushed to the right, breaking the left-right symmetry, as displayed in Fig. 3(b). A closer look at the figure reveals that the asymmetry of the ionic current distribution appears further away from the tip, whereas the near-field ionic current maintains symmetry. Even in the far field, the field strength remains above 10^4 V/m, yielding an ionic field-driven velocity (>1.4 m/s) exceeding the gas velocity. Therefore, the ionic current can be measured upstream of the tip at the bottom of the discharging zone. In comparison with Figs. 5(b), Fig. 7(b) shows that the active zone of the ionic current (pale blue) is compressed by the gas flow opposing the ionic current when the brush tip faces left. Fig. 7(c) shows the opposite trend when the carbon brush faces to the right.

Fig. 8 shows the current density profiles measured at the bottom of the discharging zone according to the orientation of the brush tip when $V_{in} = 1$ m/s. For the left-facing carbon brush, the skewness of the profile shown in Fig. 6 was alleviated by returning the peak position to $x = 0$. We presume that ions initially emitted left from the tip are forced by the opposing gas flow to turn back ahead of the tip and these ions subsequently move toward the bottom and downstream areas. This behavior of ions in the presence of gas flow is consistent with the compression of the active zone, as shown in Fig. 7(b). This leads to a reduction in the number of ions reaching the far negative x region ($x < 0$) on the bottom and an increase in the number of ions detected in the remaining areas of the bottom ($x \geq 0$), relative to the corresponding case shown in Fig. 6. However, the gas flow always accelerates the ions downstream in the case of the right-facing carbon brush, which lowers most of the ion currents measured at the bottom, except for those downstream. Fig. S3 in the Supplementary Data confirms this explanation of the ionic behavior. We selected the left-facing arrangement of the carbon brush, considering its spatially uniform ion current distribution and intense ionic current in the discharging zone.

3.2. Design characteristics of collection plates for the removal of ultrafine particles

We systematically investigated the performance of collection plates with two design parameters, operating at a high voltage for the removal of poly-disperse ultrafine particles (see Fig. S1). Specifically, the gap between two successive plates (or pitch p_{pl}), the length of the plates (L_{pl}), and the high voltage supplied to these components (φ_{pl}), as summarized

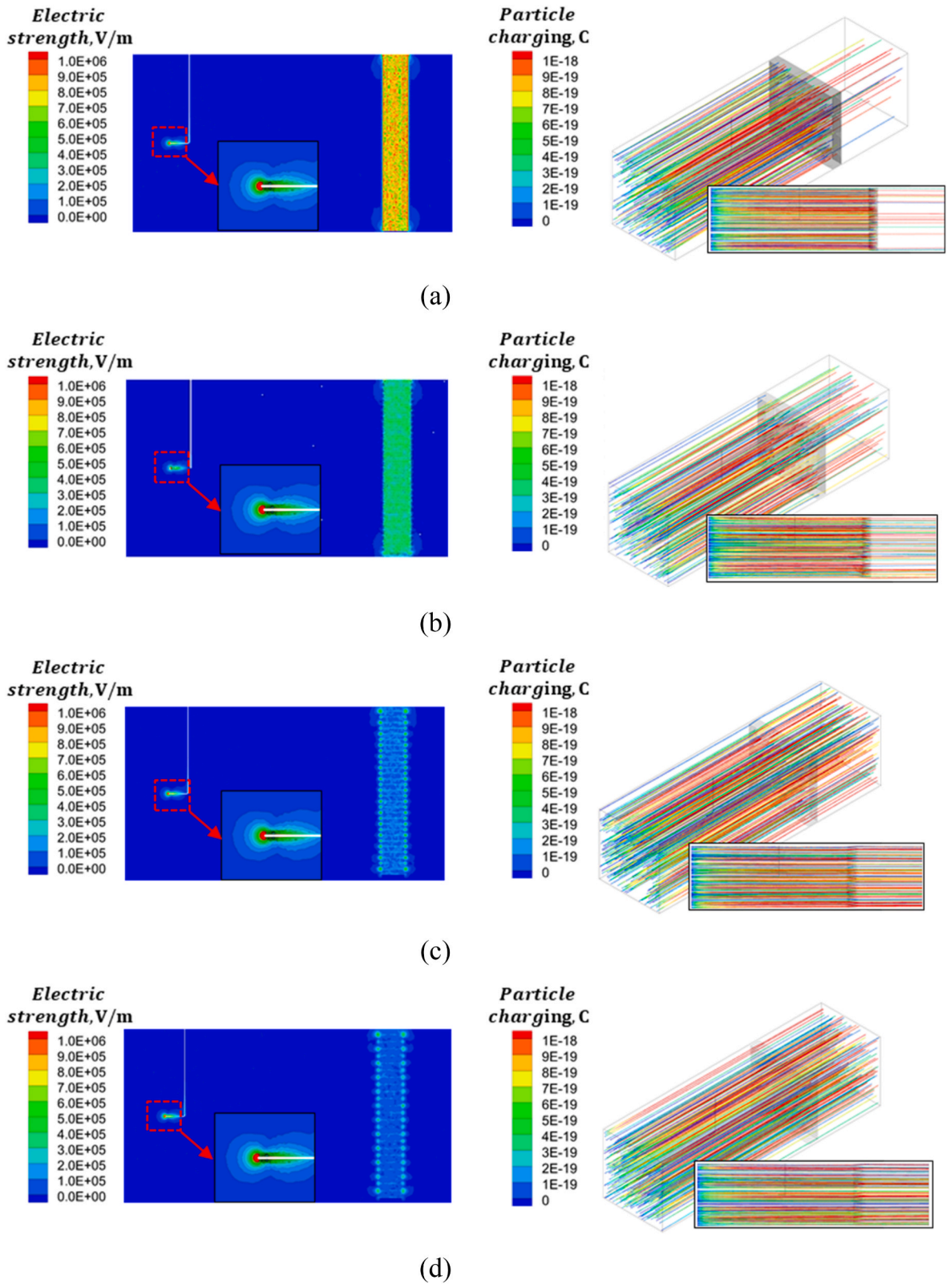

Fig. 9. Distributions of electric field strength and particle trajectories for different pitches of collecting plate: (a) $p_{pl} = 2$ mm, (b) $p_{pl} = 4$ mm, (c) $p_{pl} = 6$ mm, and (d) $p_{pl} = 8$ mm.

in Table 3. All the results shown in this section were obtained for the left-facing carbon brush in the presence of an air flow at $V_{in} = 1$ m/s with the discharging voltage fixed at −7.7 kV.

Fig. 9 shows the electric field strength and particle trajectory distribution for a gap range of 2–8 mm. As expected, when the gap decreases (from Fig. 9(d)–9(a)), the electric field strength that accumulates in the collection-plate unit increases; the number of particles passing through the collection plates decreases accordingly, as shown in the

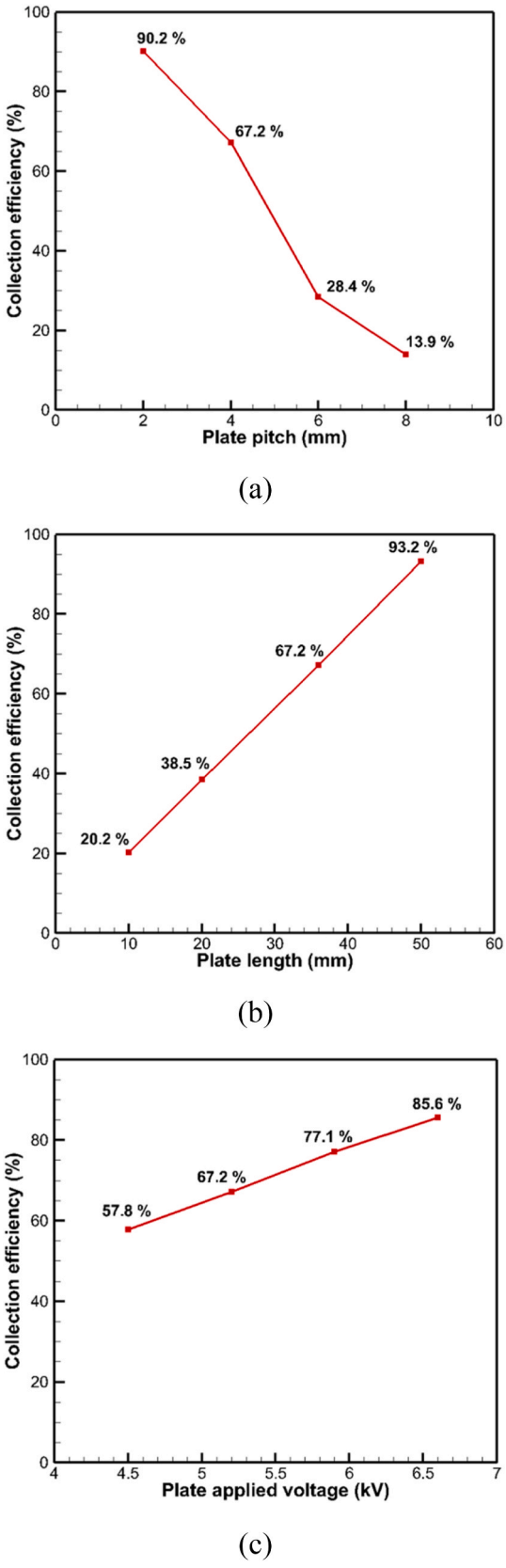

Fig. 10. Variations of collection efficiency of ultrafine particles by design/operation parameters of the particle collecting plate: (a) Pitch and (b) Length of the collecting plate, and (c) High voltage applied to the collecting plate.

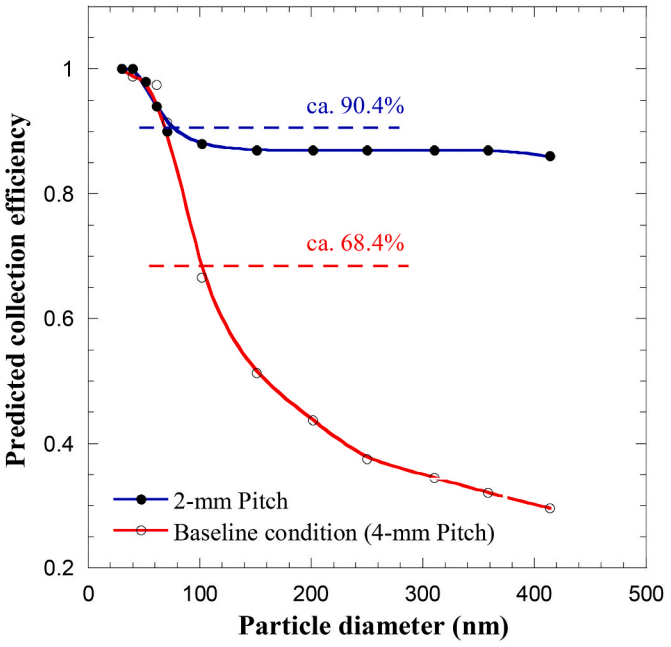

Fig. 11. Comparison of collection efficiencies per each size of ultrafine particles simulated for 2-mm and 4-mm pitch of the collection plates under the baseline condition.

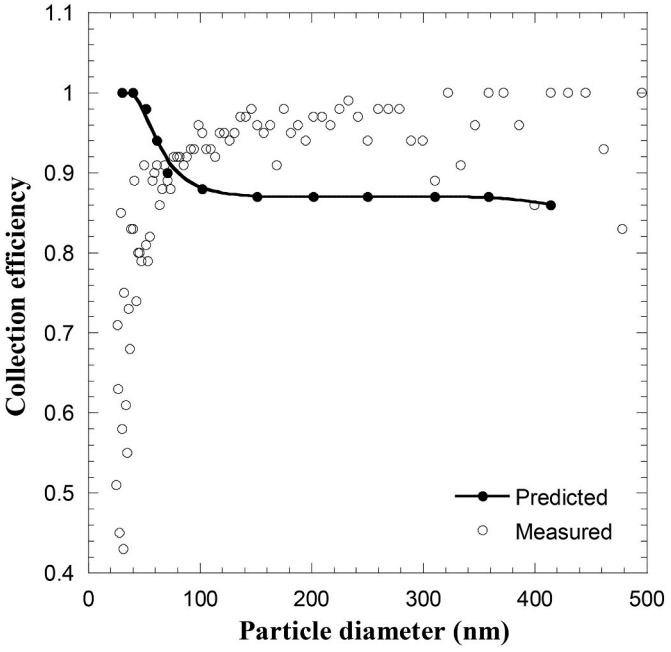

Fig. 12. Comparison of size-resolved collection efficiencies between the simulation and experiment for 2-mm pitch of the collection plates under the baseline condition.

figures on the right-hand side. This indicates a continuous increase in the particle-collection efficiency because the number fraction of *captured* particles with respect to their original number defines the particle-collection efficiency. Fig. 10(a) confirms this result. Fig. 10(b) shows the variation in the particle-collection efficiency by changing the plate length from 10 mm to 50 mm with reference to the "baseline" condition listed in Table 3. The collection efficiency increased linearly with increasing length. Similarly, Fig. 10(c) shows that the collection efficiency increased linearly with increasing the high voltage on the

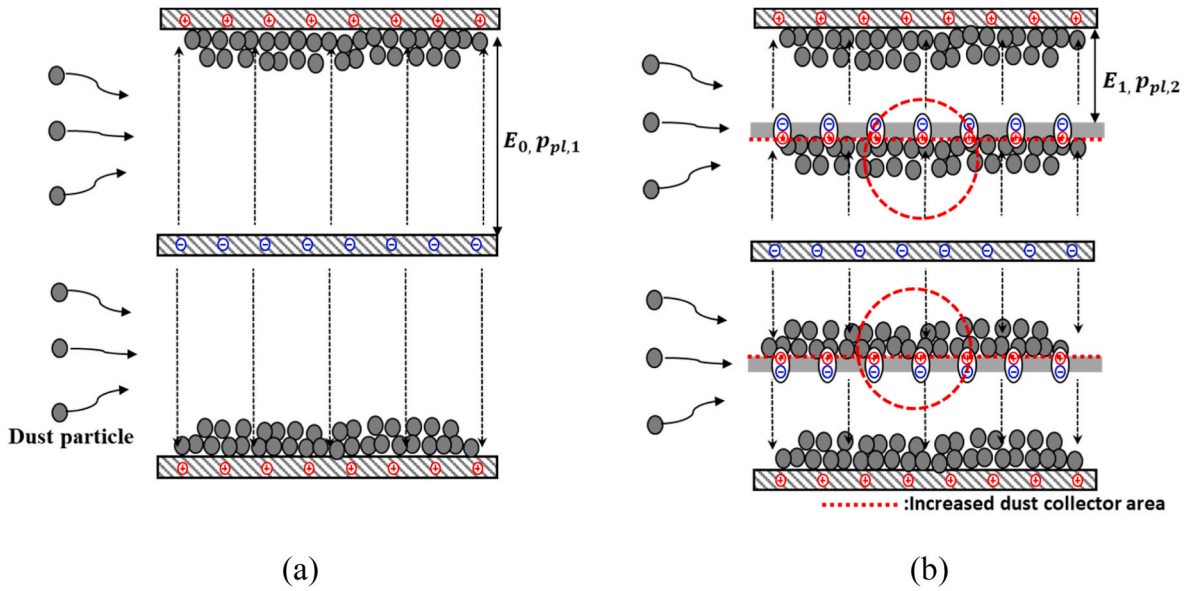

Fig. 13. Schematic illustrating the deposition of charged particles in (a) a conventional particle collection plate unit and (b) a new collection plate unit with the dielectric separator.

collection plates. All the results observed from Fig. 10(a)-10(c) indicates that the plate is too short or that the high voltage of 5.2 kV is not high enough to capture all the charged particles. Fig. 10(c) shows that using 6.6 kV for the plates with a 4 mm gap yields a collection efficiency of 85.6%, which is still lower than the efficiency of 93.2% shown in Fig. 10 (b). This suggests that there is room for further increasing the collection efficiency, for instance, by applying 6.6 kV or more to the collection plates at $p_{pl} = 2$ mm.

One may be more interested in prediction of collection efficiency as a function of particle size. We calculated the size-resolved collection efficiencies for 2-mm and 4-mm pitches under the baseline condition (Section 2.2) and compared them in Fig. 11. As a result, the size-dependent collection efficiency with $p_{pl} = 4$ mm was considerably decreased from 100% to 30% upon increasing the size from 0.03 μm to 0.41 μm, whereas the collection efficiency with $p_{pl} = 2$ mm was almost independent of particle size except for <0.1 μm. Overall collection efficiency can be estimated by taking a number-weighted average of the collection efficiency (seen in Fig. 11), accounting for the log-normal number size distribution of the particles in Fig. S2. The estimated values (as marked with dotted lines in Fig. 11) are 90.4% and 68.4%, being in good agreement with 90.2% and 67.2% in Fig. 10(a), for the cases of $p_{pl} = 2$ and 4 mm, respectively. From the perspective of particle charging, however, it is awkward that 30-nm particles, known to always undergo a poor diffusion charging, can be captured with 100% efficiency in Fig. 11.

Thus, we further examined the validity of the simulation in comparison with experimental data, with focus on the size-resolved collection efficiency. It should be noted that the collection plate unit used for the experiment was provided by a Korean company under contract, so only two types of the collection plate unit were available: One is a conventional collection plate unit with $p_{pl} = 2$ mm and $L_{pl} = 3.6$ cm; the other is a dielectrics-employed collection plate unit with $p_{pl} = 3$ mm and $L_{pl} = 3.6$ cm. In comparison with Table 3, only one case among 10 cases in Fig. 10 matched with the experiment ($p_{pl} = 2$ mm and $\varphi_{pl} =$ 5.2 kV). For this case, we measured size distributions of ultrafine particles at the sampling zone upon switching the high voltages of both ionizer and collection plates on and off, and then directly compare the results at each size to calculate the corresponding collection efficiency.

Fig. 12 compares the measured collection efficiency data with the predicted profile shown in Fig. 11. Overall, the experimental data shows the opposite trend in that small particles are less efficiently captured than larger ones. In principle, small particles, *once charged*, should be more effectively captured under the constant E field. On the other hand, the experiment displayed a cliff descent when particles <0.08 μm, meaning that small particles are less efficiently charged than bigger ones. This speculation seems more plausible in view of diffusion charging of ultrafine particles. Another notable point is that the current simulation tends to underestimate charging of particles >0.1 μm with respect to the experimental data, but overestimate charging of particles <0.1 μm. What follows is to clarify the validity of Lawless charging model in two distinct ranges of particle size.

When it comes to diffusion charging of ultrafine particles [33], Fuch's model (1963) was known to be one of the best model to calculate the combination coefficient for (*pure*) diffusion charging of particles in the transition regime at STP ($d_p > 0.03$ μm), by extending the Maxwell's limiting-sphere concept. In connection with the stochastic birth-and-death model, Fuch's model has been widely used to calculate the charging rate and charge distributions of those particles. However, the model is basically 1-D limiting sphere model that is working best for pure diffusion charging in the absence of external field. Here, Marquard [33] developed a new 2-D limiting sphere model to consider the variations of electrical potentials and spatial ion distributions around a single particle in the presence of external field. This corresponds to the combined (field and diffusion) charging that is the case in our study. More importantly, Marquard compared their model with Lawless model and stated that Lawless model has two major simplifications that may impair its application to the transition regime: one simplification relates to the neglect of the image potential, leading to *underestimation* of particle charge especially for low charge levels; the other is that Lawless model is based on continuum regime, so the lack of free-molecular consideration on particle surface leads to *overestimation* of particle charge. His notable result was that Lawless model yields an obvious *overestimation* of charge of 0.03-μm particles, which might explain the large discrepancy in collection efficiency of particles <0.08 μm shown in Fig. 12. Moreover, the former effect is speculated to link with the underestimated collection efficiency of particles >0.1 μm by simulation against the experiment (in Fig. 12), because the factor of $N_{ion} \bullet t$ in our discharging zone was low in the order of 10^{11} s/m^3, not so high as deactivating the image potential. According to Long and Yao [34] who tested various particle charging models with FLUENT, Lawless model indeed underestimates charge of submicron particles (0.18–0.28 μm) with respect to the experiment (see

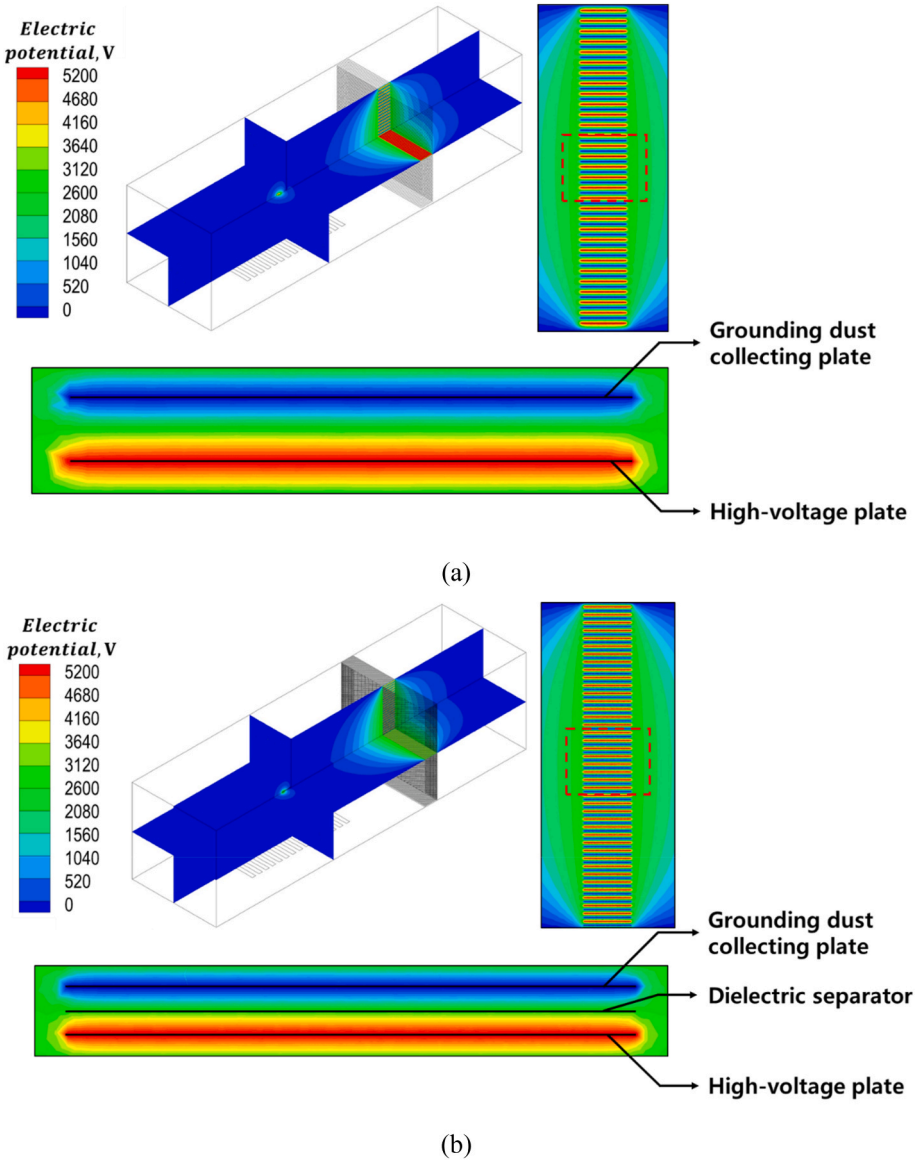

Fig. 14. Comparison of electric potential distribution between (a) the conventional particle collecting plate and (b) the new collection plate with dielectric separator.

Figs. 2 and 3 in Ref. [34]). Returning to Fig. 12, nevertheless, we believe that our simulation enables a reasonable prediction of *overall* collection efficiency of ultrafine particles (equally around 90%) by canceling out the positive and negative discrepancy through averaging.

3.3. Performance assessment of particle-collection plates with dielectric separators

We examined the effect of a dielectric separator sandwiched between two successive collection plates, a configuration recently considered in the Korean industry. Fig. 13 schematically illustrates the behavior change of charged particles with the insertion of the dielectric separator. In conventional particle-collection plates, negatively charged particles are deposited on the upper and lower plates, as shown in Fig. 13(a), owing to the corresponding upward and downward electrical forces. When a dielectric layer is inserted between the two plates, the dielectric material exhibits uniform polarization, giving rise to surface polarization charges with opposite polarities, as depicted in Fig. 13(b). The electric field strength increases in the air channel but decreases in the dielectric layer compared to the levels without the dielectric [35]. As the electric field in the air channel is of interest for the removal of charged particles, it can facilitate the efficient removal of particles. In addition, inserting a dielectric layer is known to increase the breakdown voltage to prevent overcurrent and provide additional surfaces for collecting particles, as shown in Fig. 13(b).

Despite the significant potential of dielectric materials, relatively few experimental studies have been conducted [14,15]. Therefore, we studied the electrostatic theory with dielectrics developed thus far in an effort to understand parallel-plate capacitors with dielectrics and developed a set of equations to predict the electrical potentials that accumulate on both sides of the dielectric separator. Using Eqs. (A4-A5) and the procedure described in the Appendix, we determined the electrical potential on both sides of the dielectric separator and simulated the electric field and behavior of the charged particles on the collection plates with and without the dielectric separator. For comparison, the reference collection plates without dielectrics were set such that $p_{pl} = 2$ mm, which led to the best performance (Section 3.2). In contrast, the collection plates with the inserted dielectric were set to have a thin dielectric layer ($b = 0.1$ mm) in the middle between two successive plates with $p_{pl} = 3$ mm and $L_{pl} = 3.6$ cm, as depicted in Fig. A1. In this experiment, because the high voltage φ_{pl} was maintained at 5.2 kV in both cases, the charged particles would be subjected to a lower electric

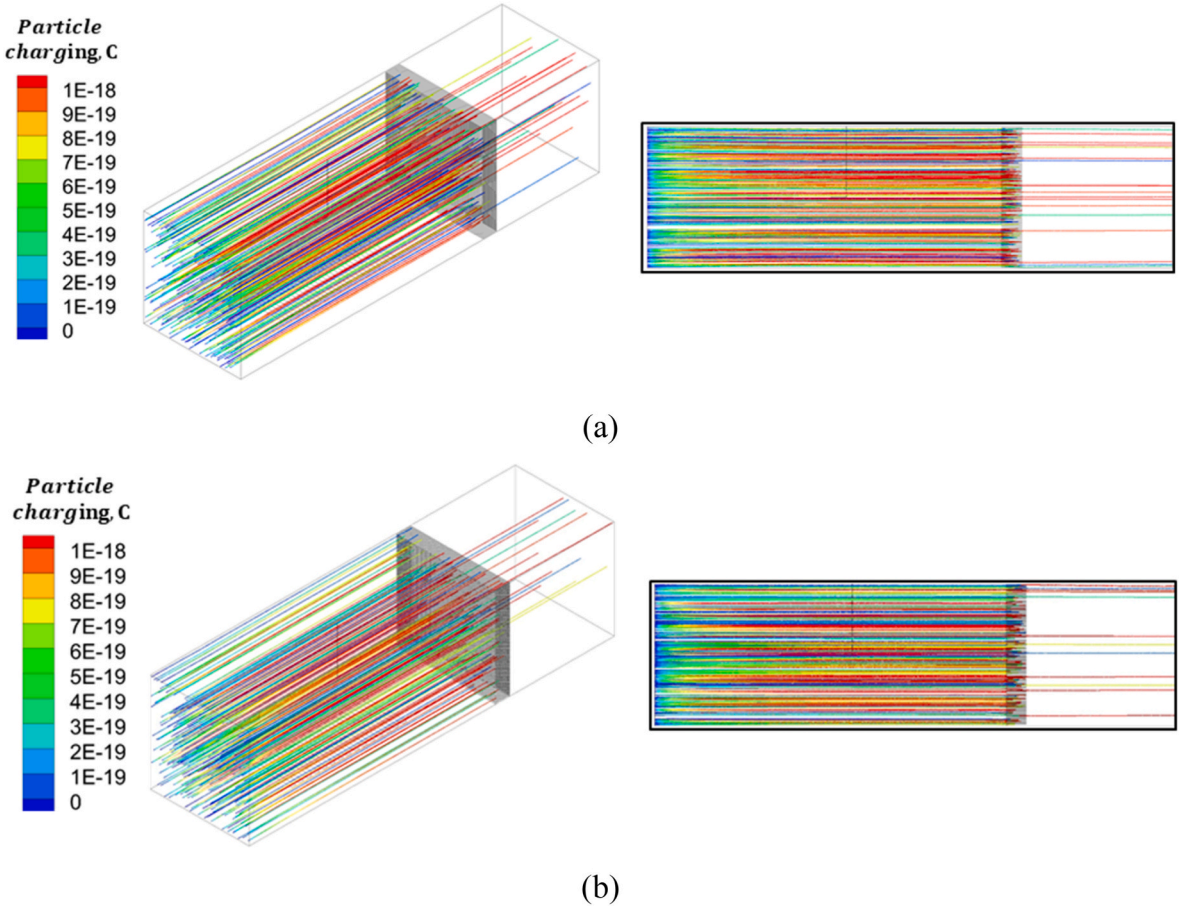

Fig. 15. Comparison of particle trajectories between (a) the conventional particle collecting plate and (b) the new collection plate with dielectric separator.

field with the dielectric compared to the case without the dielectric.

Fig. 14 compares the contour plots of the electric potential in the particle-collection plates with and without the dielectric separator. In Fig. 14(a), the figures on the upper left and right show an isometric view of the entire two-stage ESP and an enlarged side view around the collection plate assembly. The bottom figure shows a magnified view of the unit pair of the collecting plates. Fig. 14(b) presents three different views of the electric field in the collection plates with the dielectric. The isopotential lines inside the collection plates are horizontal and parallel to the plates, indicating a one-dimensional electric field in both cases. In addition, the electric potential induced on the dielectric is approximately half of the high-voltage φ_{pl}, as evident from Eqs. (A4-A5). As $b \rightarrow 0$, E_1 and E_3 equally approach E_0 without the dielectric. This implies that the use of a thin dielectric separator is undesirable, because it does not induce any difference in the electric field.

Considering this, we examined Fig. 15, which shows a noticeable difference in particle trajectories with and without a thin dielectric. Fig. 15(b) shows that even with a weaker electric field ($p_{pl} = 3$ mm vs 2 mm), the insertion of the dielectric clearly facilitates the removal of charged ultrafine particles. We repeated these numerical simulations for $\varphi_{pl} = 7.7$ kV and correspondingly conducted the experiments for comparison. Fig. 16(a) shows the size distributions of the pristine particles (measured by switching off the ionizer and collection plates) and survived particles passing through the collection plates with and without dielectric separators at 5.2 or 7.7 kV. Based on the size distribution of pristine particles, the results of survived particles demonstrate that small particles tend to be less captured than larger ones, irrespective of the existence of dielectric layers, suggesting that a poor charging of small particles does matter. Fig. 16(b) compares the collection efficiency profiles corresponding to the four cases. It is noteworthy that all data points are approximately collapsed into a single line in a range of <0.08 μm; this universal behavior represents that the collection performance is hardly affected by electric field built in the collection plates, but rather determined by the charger performance. When increasing the size of particles further, the data begin to be scattered in the cases of 5.2-kV high voltage, however this behavior is completely eliminated at 7.7 kV, suggesting that all the particles larger than 0.1 μm are completely ionized and removed by the present ESP system.

Last, let us summarize the overall collection efficiency obtained from the simulations in comparison with the foregoing experiments for each case. Without the dielectric, at $\varphi_{pl} = 5.2$ kV, the overall collection efficiency obtained from the numerical simulation and the experiment were both 90%. The efficiency increased to 95% in the experiment and 100% in the simulation at $\varphi_{pl} = 7.7$ kV. With a dielectric, the particle-collection efficiency with $\varphi_{pl} = 5.2$ kV was 93% in the experiment and 96% in the simulation. At $\varphi_{pl} = 7.7$ kV, the efficiencies were 97% and 100% in the experiment and simulation, respectively. We also measured the average charge number of the particles from the experiment in accordance with the procedure described in Section 2.1. The measured charge number of the particles was 1.7, which is slightly lower than the value of 2.3 from the numerical simulation. Despite an overestimation of a few percent in the numerical simulation, it is evident that the present numerical simulation can reasonably predict the improvement in the overall collection efficiency with the insertion of a dielectric separator.

4. Conclusions

In this study, we developed a numerical methodology based on FLUENT. This method is easy to use, and using it, we developed the first comprehensive numerical simulation for a complete two-stage ESP

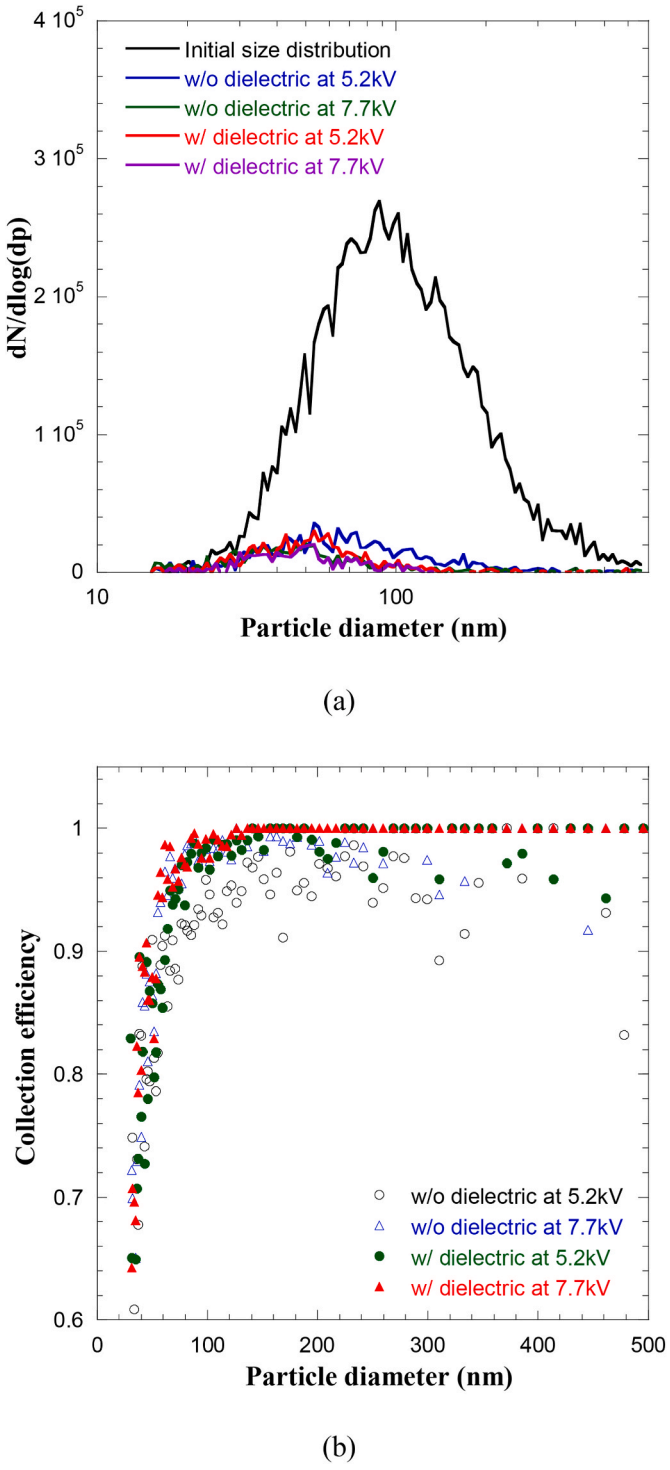

Fig. 16. Effects of high voltages and the presence of dielectrics in the collection plates on (a) number size distributions and (b) size-resolved collection efficiency of particles.

system equipped with a carbon brush ionizer. Since there was no existing experimental study on carbon brush-employed (single-stage or two-stage) full-scale ESPs for the residential use, we also developed our own ESP-duct assembly to validate the numerical simulations. We calculated the spatial distributions of the electric potential and ionic charge density, turbulent gas flow field coupled with ionic currents, charge states, and behavior of ultrafine particles in the entire region of the system. Our results showed that the orientation of the carbon brush tip with respect to the gas flow direction displayed directional emission of ions from the tip, which was confirmed experimentally. We recommend that when the carbon-brush ionizer is installed it face upstream to ensure that the ionic streams are spatially uniform in the discharging zone. The collection efficiency of ultrafine particles greatly increased with an increase in the high voltage applied to the collecting plates. A decrease in the pitch between the plates, as expected, improved the collection efficiency as well. It was observed that the length of the plates also affected the collection efficiency, suggesting that the length considered, in this study, was not sufficient to capture all of the charged particles. Finally, we examined the inclusion of a dielectric separator with the aim of doubling the active collection area and proving its positive effect by developing a new model. Through a comparative analysis between the simulations and experiments, it was determined that installing a single carbon-brush ionizer was sufficient to achieve 100% charging (and collection) efficiency for particles larger than 0.1 μm, but displayed a sharp descent in charging efficiency for smaller particles. In the whole cases considered, the present numerical simulation was proved to enable a reasonable prediction of overall collection efficiency of ultrafine particles. In terms of practicality, we summarize the distinct difference of our ESP from other types reported in literatures: 1) a single carbon brush ionizer that is about a few dollars in market is enough to treat the 1-m/s dusty air through the duct with a cross section of 25 cm × 25 cm, whereas a larger number of wire-plate ionizer units are required to cover the cross section; 2) a carbon brush that is a bundle of 7-μm ultrathin carbon wires is more efficient for charging ultrafine particles with less emission of ozone compared with the other types including wire-plate or point-plate ionizers.

CRediT authorship contribution statement

Sehyun Kim: Writing – original draft, Formal analysis. **Kiwoong Park:** Validation, Formal analysis. **Changyoung Choi:** Resources, Project administration, Conceptualization. **Man Yeong Ha:** Writing – review & editing, Supervision, Software, Resources, Project administration, Conceptualization. **Donggeun Lee:** Writing – review & editing, Validation, Supervision, Resources, Project administration, Funding acquisition, Conceptualization.

Declaration of competing interest

The authors declare that they have no known competing financial interests or personal relationships that could have appeared to influence the work reported in this paper.

Data availability

The authors do not have permission to share data.

Acknowledgments

This research was supported by the National Research Foundation of Korea (NRF) grant funded by the Korea government (MSIT) (NRF2019R1A5A8083201), Basic Science Research Program through the National Research Foundation of Korea (NRF) funded by the Ministry of Education (NRF-2020R1A2C2011634), and LG Electronics.

Appendix A. Supplementary data

Supplementary data to this article can be found online at https://doi.org/10.1016/j.buildenv.2022.109493.

Appendix. Mathematical expressions for the numerical simulation of collection plates with dielectrics

Fig. A1 illustrates how an electric field develops between two identical metallic plates with and without a dielectric layer. Without a dielectric, when a high voltage of φ_{pl} is applied to the upper plate while the bottom plate is grounded, we obtain a spatially uniform electric field with a field strength of $E_0 = \varphi_{pl}/P_{pl}$. Applying Gauss's law, the field strength is directly related to the total (free) charge density on each plate $\sigma_{free,0}$ according to $E_0 = \sigma_{free,0}/\varepsilon_0$, where ε_0 is the air permittivity. All variables and constants appearing in the Appendix have SI units.

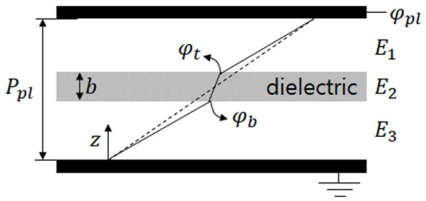

Fig. A1. Schematic of electric field developed in the collection plates with and without a dielectric separator.

When a dielectric layer with thickness of b was inserted between the plates, as shown in Fig. A1, the electric field induces dipole moments in the dielectric such that the electric field E_2 is lower than the original value E_0 without the dielectric, which in turn increases the electric field between the plate and dielectrics E_1 and E_3 beyond the value of E_0 (as depicted in Fig. A1). The voltage between the plates is the integral of the electric field, which is divided into three zones. Because each field is uniform, the voltage of the upper plate φ_{pl} is simply the sum of the product of the electric field and the distance between the three zones, as follows:

$$\varphi_{pl} = E_1(P_{pl} - b) + E_2 b = \frac{\sigma_{free}}{\varepsilon_0}(P_{pl} - b) + \frac{\sigma_{free}}{\varepsilon_r \varepsilon_0} b = \frac{\sigma_{free}}{\varepsilon_0}\left[P_{pl} - b\left(1 - \frac{1}{\varepsilon_r}\right)\right] \tag{A1}$$

Here, σ_{free} is the (free) charge density at each plate and ε_r is the dielectric constant of the dielectric layer. It should be noted that $E_1 = E_3$ because the net charge in the dielectric is zero, and the equations for E_0 can provide another equation for φ_{pl}, as follows:

$$\varphi_{pl} = E_0 P_{pl} = \frac{\sigma_{free,0}}{\varepsilon_0} P_{pl} \tag{A2}$$

Equating Eqs. (A1 and A2), the charge density σ_{free} is expressed in relation to $\sigma_{free,0}$ as

$$\sigma_{free} = \sigma_{free,0} \frac{P_{pl}}{P_{pl} - b\left(1 - \frac{1}{\varepsilon_r}\right)}. \tag{A3}$$

Given that $\varepsilon_r > 1$, Eq. (A3) indicates that $\sigma_{free} > \sigma_{free,0}$ and the total charge stored in the system is always larger than it would be without a dielectric, as $Q > Q_0$ by $Q = \sigma_{free} A$ and $Q_0 = \sigma_{free,0} A$, where A is the area of the plate. Based on the basic equations for a capacitor, the values of the electric potential on the top and bottom surface of the dielectric (φ_t and φ_b, respectively) can be obtained using well-defined parameters and Eq. (A4) and (A5), respectively.

$$\varphi_b = E_1 \frac{1}{2}(P_{pl} - b) = E_0 \frac{P_{pl}}{P_{pl} - b\left(1 - \frac{1}{\varepsilon_r}\right)} \frac{1}{2}(P_{pl} - b) \tag{A4}$$

$$\varphi_t = \varphi_b + E_2 \mathrm{b} = E_0 \frac{P_{pl}}{P_{pl} - b\left(1 - \frac{1}{\varepsilon_r}\right)} \left[\frac{1}{2}(P_{pl} - b) + \frac{b}{\varepsilon_r}\right] \tag{A5}$$

For instance, for the given condition of $\varepsilon_r = 10$, $d = 3$ mm, $b = 1$ mm, $\varphi_{pl} = 5.2$ kV, and $A = 90$ cm^2, φ_b and φ_t are calculated and found to be 2476 and 2724 V, respectively, with respect to the values of 1733 and 3467 V without the dielectric. This reconfirms that E_2 is significantly lower than E_0 in the absence of the dielectric (1.73×10^6 V/m vs 2.48×10^5 V/m), consistent with common understanding, whereas E_1 and E_3 outside the dielectric are larger than E_0. In conclusion, one may use Eqs. (A4 and A5) to define the boundary conditions, in terms of the electric potential, on both sides of the dielectric.

References

[1] H.M. Chein, S.G. Aggarwal, H.H. Wu, T.M. Chen, C.C. Huang, Field enhancements of packed-bed performance for low-concentration acidic and basic-waste gases from semiconductor manufacturing process, J. Air Waste Manage. 55 (2005) 647–657.

[2] R.W.K. Allen, A. Van Santen, Designing for pressure drop in venture scrubbers: the importance of dry pressure drop, Chem. Eng. J. Biochem. Eng. J. 61 (1996) 203–211.

[3] C.H. Huang, C.J. Tsai, Y.M. Wang, Control efficiency of submicron particles by an efficient venture scrubber system, J. Environ. Eng. 133 (2007) 454–461, 2007.

[4] C.G. Smith, T.B.F. Cottrell, Dry Electrostatic Precipitator, 1989. US04877427A.

[5] K.R. Parker, Applied Electrostatic Precipitation, Blackie Academic& Professional, London, 1997.

[6] G.A. Kallio, D.E. Stock, Interaction of electrostatic and fluid dynamic fields in wire—plate electrostatic precipitators, J. Fluid Mech. 240 (1992) 133–166.

[7] J.R. McDonald, W.B. Smith, H.W. Spencer III, A mathematical model for calculating electrical conditions in wire-duct electrostatic precipitation devices, J. Appl. Phys. 48 (1977) 2231–2243.

[8] K.S.P. Nikas, A.A. Varonos, G.C. Bergeles, Numerical simulation of the flow and the collection mechanisms inside a laboratory scale electrostatic precipitator, J. Electrost. 63 (2005) 423–443.

[9] P.A. Lawless, Particle charging bounds, symmetry relations, and an analytic charging rate model for the continuum regime, J. Aerosol Sci. 27 (1996) 191–215.

[10] H.Y. Choi, Y.G. Park, M.Y. Ha, Numerical study on the effect of staggered wire electrodes in an electrostatic precipitator, J. Mech. Sci. Technol. 34 (2020) 3303–3310.
[11] H.Y. Choi, Y.G. Park, M.Y. Ha, Numerical simulation of the wavy collecting plate effects on the performance of an electrostatic precipitator, Powder Technol. 382 (2021) 232–243.
[12] M. Gao, Y. Zhu, X. Yao, J. Shi, W. Shangguan, Dust removal performance of two-stage electrostatic precipitators and its influencing factors, Powder Technol. 348 (2019) 13–23.
[13] Y. Zhu, C. Chen, J. Shi, W. Shangguan, Enhancement of air purification by unique W-plate structure in two-stage electrostatic precipitator: a novel design for efficient capture of fine particles, Adv. Powder Technol. 31 (2020) 1643–1648.
[14] S.H. Kim, Y.H. Jang, J.Y. Bang, G.H. Sim, M.C. Park, J.K. Lee, Y.C. Ahn, Performance evaluation of the dielectric electrostatic precipitator for collecting ultra fine particles, J. Power System Eng. 24 (2020) 87–93.
[15] S.H. Kim, J.Y. Bang, J.K. Lee, M.C. Park, C.W. Kim, H.Y. Kim, J.W. Kim, C.K. Kim, Site evaluation of the dielectric electrostatic precipitator for removing ultra fine particles in the subway platform, J Korean Soc. Urban Railway 8 (2020) 719–726.
[16] H.J. Kim, B. Han, C.G. Woo, Y.J. Kim, Ozone emission and electrical characteristics of ionizers with different electrode materials, numbers, and diameters, IEEE Trans. Ind. Appl. 53 (2017) 459–465.
[17] Y.J. Kim, B.W. Han, C.G. Woo, H.J. Kim, Performance of ultrafine particle collection of a two-stage ESP using a novel mixing type carbon brush charger and parallel collection plates, IEEE Trans. Ind. Appl. 53 (2017) 466–473.
[18] H.J. Kim, M.J. Kim, B.W. Han, C.G. Woo, A. Zouaghi, N. Zouzou, Y.J. Kim, Fine particle removal by a two-stage electrostatic precipitator with multiple ion-injection-type prechargers, J. Aerosol Sci. 130 (2019) 61–75.
[19] J.H. Sung, Y.W. Lee, B.W. Han, Y.J. Kim, H.J. Kim, Improvement of particle clean air delivery rate of an ion spray electrostatic air cleaner with zero-ozone based on diffusion charging, Build. Environ. 186 (2020), 107335.
[20] P. Sattari, G.S.P. Castle, K. Adamiak, Numerical simulation of trichel pulses in a negative corona discharge in air, IEEE Trans. Ind. Appl. 47 (2011) 1935–1943.
[21] Y. Guan, R.S. Vaddi, A. Aliseda, I. Novosselov, Experimental and numerical investigation of electrohydrodynamic flow in a point-to-ring corona discharge, Phys. Rev. Fluids 3 (2018), 043701.
[22] Y. Zheng, L. Wang, D. Wang, S. Jia, Numerical study of the effect of the needle tip radius on the characteristics of Trichel pulses in negative corona discharges, Phys. Plasmas 24 (2017), 063515.
[23] D.H. Park, Y.H. Kim, S.G. Lee, C. Kim, J.H. Hwang, Y.J. Kim, Development and performance test of a micromachined unipolar charger for measurements of submicron aerosol particles having a log-normal size distribution, J. Aerosol Sci. 41 (2010) 490–500.
[24] J. Pyo, Y. Ock, D. Jeong, K. Park, D. Lee, Development of filter-free particle filtration unit utilizing condensational growth: with special emphasis on high-concentration of ultrafine particles, Build. Environ. 112 (2017) 200–208.
[25] Y. Ock, J. Kim, I. Choi, D.S. Kim, M. Choi, D. Lee, Size-independent unipolar charging of nanoparticles at high concentrations using vapor condensation and its application for improving DMA size-selection efficiency, J. Aerosol Sci. 121 (2018) 38–53.
[26] F. Greifzu, C. Kratzsch, T. Forgber, F. Lindner, R. Schwarze, Assessment of particle-tracking models for dispersed particle-laden flows implemented in OpenFOAM and ANSYS FLUENT, Eng. Appl. Comp. Fluid 10 (2015), 1104266.
[27] F.W. Peek, Dielectric Phenomena in High Voltage Engineering, McGraw-Hill Book Company, Incorporated, 1920.
[28] G.W. Penney, R.E. Matick, Potentials in D-C corona fields, Trans. Am. Inst. Electr. Eng. Part 1 79 (1960) 91–99.
[29] J. Kim, J.H. Shin, D. Lee, Microstructural transition of nanoparticle deposits from multiple dendrites to compact layer, J. Aerosol Sci. 159 (2022), 105876.
[30] ANSYS, ANSYS Fluent Theory Guide, ANSYS 15.2 Doc, 2015, p. 80, 15317.
[31] G.J. Lindquist, D.Y.H. Pui, C.J. Hogan Jr., Porous particulate film deposition in the transition regime, J. Aerosol Sci. 74 (2014) 42–51.
[32] P. Rosin, E. Rammler, The laws governing the fineness of powdered coal, J. Inst. Fuel 7 (1933) 29–36.
[33] A. Marquard, Unipolarfield and diffusion charging in the transition regime-Part I: a 2-D limiting-sphere model, Aerosol Sci. Technol. 41 (2007) 597–610.
[34] Z. Long, Q. Yao, Evaluation of various particle charging models for simulating particle dynamics in electrostatic precipitators, J. Aerosol Sci. 41 (2010) 702–718.
[35] The Feynman lecture on physics. https://www.feynmanlectures.caltech.edu/.